SHUTTLE ORBITER CONTINGENCY ABORT AERODYNAMICS: REAL-GAS EFFECTS AND HIGH ANGLES OF ATTACK

Dinesh K. Prabhu, Periklis E. Papadopoulos, Carol B. Davies,
ELORET Corp., 690 W. Fremont Ave., Suite 8, Sunnyvale, CA 94087

Michael J. Wright, Ryan D. McDaniel, Ethiraj Venkatapathy, Paul F. Wercinski
NASA Ames Research Center, Moffett Field, CA 94035

Nomenclature

c_{ref}	:	wing reference chord	T	:	static temperature
C_A	:	axial force coefficient	T_∞	:	freestream static temperature
C_m	:	pitching moment coefficient	V_∞	:	freestream speed
C_N	:	normal force coefficient	Z	:	altitude
C_p	:	surface pressure coefficient	x, y, z	:	axial, span, and normal coordinates
F_x, F_x	:	axial and normal forces	α	:	angle of attack
L_B	:	body length – from nose tip to hinge line of the body flap	γ	:	ratio of specific heats
M_y	:	pitching moment – about a y-directed axis passing through the C.G.	$\Delta\alpha$	:	angle of attack increment
M_∞	:	freestream Mach number	δ_{BF}	:	body flap deflection
p_w	:	surface pressure	δ_c	:	semi-vertex angle of a sharp cone
p_∞	:	freestream static pressure	δ_E	:	elevon deflection
q_∞	:	freestream dynamic pressure	δ_{SB}	:	speed brake deflection
Re_∞	:	freestream unit Reynolds number	$\theta_{\delta_{max}}$	:	shockwave angle for maximum flow deflection for a sharp cone or wedge
S_{ref}	:	reference planform area	ρ	:	freestream mass density

Introduction

An important element of the Space Shuttle Orbiter safety improvement plan is the improved understanding of its aerodynamic performance so as to minimize the "black zones" in the contingency abort trajectories [1]. These zones are regions in the launch trajectory where it is predicted that, due to vehicle limitations, the Orbiter will be unable to return to the launch site in a two or three engine-out scenario. Reduction of these zones requires accurate knowledge of the aerodynamic forces and moments to better assess the structural capability of the vehicle.

An interesting aspect of the contingency abort trajectories is that the Orbiter would need to achieve angles of attack as high as 60°. Such steep attitudes are much higher than those for a nominal flight trajectory. The Orbiter is currently flight certified only up to an angle of attack

of 44° at high Mach numbers and has never flown at angles of attack larger than this limit. Contingency abort trajectories are generated using the data in the Space Shuttle Operational Aerodynamic Data Book (OADB) [2]. The OADB, a detailed document of the aerodynamic environment of the current Orbiter, is primarily based on wind-tunnel measurements (over a wide Mach number and angle-of-attack range) extrapolated to flight conditions using available theories and correlations, and updated with flight data where available. For nominal flight conditions, i.e., angles of attack of less than 45°, the fidelity of the OADB is excellent due to the availability of flight data. However, at the off-nominal conditions, such as would be encountered on contingency abort trajectories, the fidelity of the OADB is less certain.

The primary aims of a recent collaborative effort (completed in the year 2001) between NASA and Boeing were to determine: 1) accurate distributions of pressure and shear loads on the Orbiter at select points in the contingency abort trajectory space; and 2) integrated aerodynamic forces and moments for the entire vehicle and the control surfaces (body flap, speed brake, and elevons). The latter served the useful purpose of verification of the aerodynamic characteristics that went into the generation of the abort trajectories.

Previous Efforts

The previous efforts of the project group at NASA Ames Research Center are briefly recapitulated here. Modern techniques of Computational Fluid Dynamics (CFD) were used to compute three-dimensional flow fields around the entire Orbiter for a run matrix that spanned critical regimes of the contingency abort trajectories. As agreed upon at the commencement of the project, solutions were computed at Mach numbers of 3.5, 6, and 15 for several angles of attack ranging from 20° to 60° (in increments of 10°), and for one angle of attack ($\alpha = 40°$) at Mach 10. The test matrix included several settings of the control surfaces (body flap, speed brake, and elevons). Fully turbulent flow solutions were computed using an ideal-gas ($\gamma=1.4$) model at Mach 3.5 and 6; and laminar solutions were computed using a real-gas (5-species air with finite-rate chemistry) model at Mach 10 and 15. In addition, a benchmark case was computed for wind-tunnel conditions of Mach 3.5 and angle of attack of 18.5°. The OADB was the basis for comparing, verifying and establishing the accuracy of the computed aerodynamic characteristics for the run matrix, and experimentally measured pressure coefficients were the basis for the benchmark case. The details of the process and methodology followed at NASA Ames Research Center, plus a complete set of results, are given in the comprehensive paper of Papadopoulos *et al*. [3]

At the start of the previous project it was expected that, apart from the effort involved in generating complex volume grids for various angles of attack and control surface settings, the work would be fairly routine – involving straightforward application of mature CFD tools to the various flight cases and extraction of pressure and shear loads for structural analysis. However, the results from the Mach 15 computations yielded a few surprises.

The angle-of-attack variations of the computed pitching moment coefficients from the Mach 6 and 15 computations3 are shown in Figs. 1a and 1b, respectively (same as Figs. 15a and 17c in Ref. 3). Also shown in the figures are the data extracted from the OADB. At Mach 6 there was good agreement, across the angle-of-attack range, between the computations and the OADB values. In particular, the computations predict a reversal in pitching moment, which is expected in the angle-of-attack range of 50° to 60°. At Mach 15, however, there was good agreement between computations (using a 5-species nonequilibrium air model) and OADB values of C_m only up to an angle of attack of 50°. More importantly, the previous computations3 do not predict a reversal in pitching moment beyond this angle of attack. Further, at $\alpha = 60°$, the difference between the computed and the OADB values of Cm was substantial. The difference in C_m has serious implications – the aerodynamic forces required to statically trim ($C_m = 0$) the vehicle at $\alpha = 60°$ are much larger than would be expected based on the OADB. In Ref. 3 the lack of pitching moment reversal for $50° \leq \alpha \leq 60°$ in Mach 15 computations was attributed to real-gas effects and a limited number of ideal-gas computations were performed at Mach 15 as a confirmation. However, the granularity in the angle of attack ($\Delta\alpha = 10°$) was insufficient to obtain a more precise location of the pitching moment reversal. It must be noted that after the first Shuttle flight, the real-gas influence on the aerodynamic characteristics of the Orbiter at high Mach numbers was thoroughly investigated by several researchers [4, 5] using physical models appropriate to the flow regime. These efforts led to the incorporation into the OADB, of increments in the aerodynamic force and moment coefficients due to real-gas effects. However, these previous analyses were limited to angles of attack of less than 45°.

Objectives

The mission-critical application of the previously computed results underscores the importance of establishing their credibility and accuracy. Establishing this credibility is the primary goal of the present work. A second objective of the paper is to investigate thoroughly real-gas effects and their impact on the Orbiter aerodynamics at large angles of attack. A third objective is to examine the viability of experimental testing in a CF_4 facility to replicate flight aerodynamics with real-gas effects.

The strategy adopted in the present work is to compute a large number of cases in the hypersonic regime with both ideal- and real-gas models using coarsened versions of volume grids that were used in the previous computations [3]. The results of the ideal-gas computations are compared against experimental data wherever possible. For a given Mach number, the ideal- and real-gas results are compared at several angles of attack to determine the impact of real-gas effects on the pitching moment and its reversal, if any. The validity of a 1970s heuristic argument used to predict the pitching moment reversal is verified through ideal-gas computations, and extended through real-gas computations, over sharp cones.

Methodology

Configuration

Figure 2 shows the Orbiter configuration, the coordinate system, and sign conventions for the positive aerodynamic forces (C_N and C_A) and the pitching moment (C_m), used in the present work. Note that there are no engine details in the aft section of the vehicle and the engines have been covered [3]. This simplification to the vehicle configuration prevents excessive complexity in the three-dimensional volume grid topology. It must also be noted that the windward, side, and trailing edges of the body flap are exactly preserved from the original geometry while the leeward side is covered in the simplification.

Computational Tool and Physical Models

Version 3.2.4 of the commercially available code, *GASPex* [6] developed by AeroSoft, Inc., is used in all of the simulations performed in the present work. This CFD code was also used in the earlier work of Papadopoulos et al. [3] Information about the physical and numerical modeling options exercised in *GASPex* is summarized in Table 1. The choice of numerical algorithm is based on the experience gained from previous projects [7, 8].

Five gas models are considered in the present work.
  A. <u>Ideal gas</u>: The flow medium is a single species gas whose ratio of specific heats (γ) is a constant. For air as an ideal gas, this ratio has a value of 1.4. Results from this model form the basis for comparison.
  B. <u>Non-reacting mixture of ideal gases</u>: The flow medium is 5-species air (N_2, O_2, NO, N, and O) in which no chemical reactions between the constituent species are allowed. In this model, the diatomic species are assumed to be rigid rotors. The ratio of specific heats (γ) of each species and that of the mixture are constants. Strictly speaking, the lack of chemical reactions reduces the number of species from 5 to 2 – only N_2 and O_2 need to be considered. Since this model is exercised in only two cases, the additional species (hence, the additional mass conservation equations) are included.
  C. <u>Non-reacting mixture of perfect gases</u>: The flow medium is again 5-species air in which no chemical reactions between the constituent species are allowed. In this model, however, the diatomic species are assumed to be simple harmonic oscillators. Based on equilibrium statistical mechanics, the specific heats (at constant pressure and at constant volume) of the diatomic species are nonlinear functions of temperature. Consequently, the ratio of specific heats (γ) of each diatomic species and that of the mixture are also nonlinear functions of temperature.
  D. <u>Real gas</u>: This gas model is the same as Model C above, however, chemical reactions between the constituent species are allowed. These reactions are assumed to be finite-rate processes.

E. <u>CF$_4$ gas</u>: The flow medium is a single species gas – carbon tetrafluoride. As in Model C, the thermodynamic properties are obtained from equilibrium statistical mechanics. The specific heats (at constant pressure and at constant volume) of CF$_4$ are nonlinear functions of temperature. The coefficient of viscosity of CF$_4$ is included in the curve-fit form of Blottner *et al*. [10]. The curve-fit constants are obtained by fitting the data of Svehla [11]. Note that GASPex can handle an arbitrary number of species and reactions and introducing a new species such as CF$_4$ only involves changes to the thermochemical database and not to the core CFD methodology.

Using these gas models, three-dimensional computations are performed at three freestream Mach numbers (Mach 6, 10, and 15) and several angles of attack. The freestream conditions for the computations are given in Table 2 and the angle-of-attack schedule is given in Table 3. The pressure and shear stresses extracted from a computed solution are integrated numerically to obtain the global aerodynamic force and moment coefficients, C_N, C_A, and C_m.

Simplifying Assumptions

Combining Tables 2 and 3, it is evident that a large number of three-dimensional computations have to be performed. This test matrix represents an enormous investment in computer time and resources. In order to conserve these resources, the following simplifying assumptions were made.

1. No control surface deflections – the aim of the present work is to obtain aerodynamic forces and moments for an untrimmed configuration so that, if needed, the impact of control surfaces can be studied. Note that in the previous computations3 the speed brake was deflected outward by approximately 70° only for the Mach 3.5 and 6 cases. A detailed examination of the results of the previous work3 showed the contribution of the deflected speed brake to the vehicle pitching moment was negligibly small at very high angles of attack.
2. No new grids – generation of three-dimensional volume grids of the complexity used in the work of Papadopoulos et al. [3] was a time-consuming effort. Re-use of the existing volume grids represents substantial savings in time.
3. In the previous effort [3], all cases were computed on two levels of grid refinement using the grid-sequencing strategy in *GASPex* [6] The coarse grid was created by eliminating every other point in each coordinate direction from the fine grid. Consequently, the coarse and fine grids differed by a factor of 8 in point density. Note that the fine grid for the Shuttle Orbiter configuration in Fig. 2 contained approximately 2.2 million points. The wake grid added another 1.4 million points to the total. The surface mesh-point distributions for the coarse and fine grids are compared in Fig. 3.
4. A detailed examination of the results of the grid studies performed in Ref. 3 showed that the coarse grids yielded small changes in normal force and pitching moment coefficients and slightly larger changes in the axial force coefficients. All differences between the

results of the fine and coarse grids were less than the corresponding OADB uncertainties. The fact that the coarse grids did not substantially change the predicted vehicle pitching moments is used to justify relying upon a large number of coarse-grid computations (a significant savings in both time and computer resources) in the present work.

5. Wake grids – Although expected to be small at hypersonic Mach numbers, the contribution of the base is included for all angles of attack by including a wake grid in the simulations.

6. Hypersonic Mach numbers only – the Mach 3.5 cases are not included in the present work.

7. Laminar flow only – a detailed examination of the results of the previous work3 led to the observation that at hypersonic Mach numbers, the contribution of the surface shear (either laminar or turbulent) was largely to the axial force (also see Ref. 9). Since the focus of the present work is the vehicle pitching moment, it is sufficient to assume the flow to be laminar. This choice reduces the computational time by a small fraction.

8. Fixed wall temperature – the focus of the present work is on the aerodynamic environments and not on the aerothermodynamic environments. Therefore, the time-consuming radiative equilibrium wall boundary condition employed in Ref. 3 is replaced by a simpler isothermal wall boundary condition. The impact of the changed surface boundary condition was examined in Ref. 9 and found to have no significant impact on the predicted aerodynamic force and moment coefficients.

9. More ideal gas solutions than real gas solutions – the computed aerodynamic forces and moments from the ideal-gas computations can be compared against data obtained from ground-based facilities. Also, ideal-gas solutions are much quicker (and hence cheaper) to compute than real-gas solutions.

Ideal Gas Model: Experimental Verification

Based on the lessons learned from the grid refinement studies, a large number of ideal-gas cases (covering an angle-of-attack range from 0° to 70°) at Mach 6, 10, and 15 are computed on coarse grids for the full-scale Orbiter configuration. Confidence in the ability of *GASPex* to predict the overall vehicle aerodynamics in ideal-gas flow regimes can be enhanced through comparison against data from wind-tunnel experiments. Due to low operating freestream enthalpies, most hypersonic wind tunnels cannot replicate the true flight environment (dominated by real-gas effects at very high Mach numbers). However, these facilities do provide good data for verifying ideal-gas results.

There is a wealth of data from the extensive experimental program that was employed in the design and development of the Orbiter. Some of the experiments were performed for scaled-Orbiter models at very high angles of attack ($\alpha \geq 60°$). However, for the Mach number regime of current interest ($M\infty \geq 6$), ready access to experimental data proved to be difficult. The catalog of Romere and Brown [12] was useful in identifying potential candidates for

experimental data. One such candidate was Test OA258 in which aerodynamic measurements for a 0.02-scale model of the Orbiter were made at Mach 6 ($\delta_{SB} = 0°$) in the Von Kármán Tunnel B at AEDC. As direct access to the relevant report was not possible, the data for this experiment were electronically extracted from the Orbiter Aerodynamic Design Substantiation Report [13]. The computed pitching moment data at Mach 6 are compared against the measured values [13] in Fig. 4. Also shown in the figure are pitching moment values extracted from the OADB. There is excellent agreement between computation and experiment (OA258) although the OADB values are somewhat different from both. Since the OADB is a collection of data from many different sources, the difference is not a significant concern. It should be noted that the computational results and experimental data clearly show a pitching moment reversal between the angles of 50° and 60°.

A second, and more recent, set of measurements are due to Paulson and Brauckmann [14]. They considered 0.004 and 0.0075-scale models in the Mach 6 (Air) and Mach 10 (Air) tunnels at NASA Langley Research Center (LaRC). In Figs. 5, the computed pitching moment coefficients at Mach 6 are compared against both measured values and OADB data. The measured pitching moment coefficients are in good agreement. The experimental data are in better agreement with the OADB values than those from Test OA258. The computations do follow the trend in the experimental data. The measurements, unfortunately, do not go beyond 45° and consequently do not show a reversal in pitching moment. The computed pitching moment coefficients at Mach 10 are compared against both measured values and OADB data in Figs. 6. As in the Mach 6 case, the present computations follow the experimental trends quite closely. Further, the computations clearly show a reversal in pitching moment in the angle-of-attack range of 50°–60°. The pitching moment data extracted from the OADB are significantly different from both the ideal-gas computations and measurements. In the previous work [3], the computed real-gas pitching moment at Mach 10 showed good agreement with the OADB value at an angle of attack of 40° – a flight measurement.

Note that in all comparisons made above, the computed data are for the full-scale Orbiter and the experimental data are for scaled models, i.e, the Reynolds numbers of the flight cases and experiments are not the same. Since the impact of the surface shear on the aerodynamics is expected to be small (except in axial force) at hypersonic Mach numbers, the disparity in the Reynolds numbers is not of any significant concern. The agreement between computations and measurements gives confidence in the dynamic (i.e., Mach number) similarity between the flow over a geometrically scaled model and that over the full-scale vehicle.

The results from the ideal-gas computations lead to the following observations: (1) the ideal-gas model behaves as expected and provides results that closely follow the experimental data up to $\alpha = 60°$ for Mach 6 and up to $\alpha = 45°$ for Mach 10; (2) the computed pitching moments clearly show a reversal in the angle-of-attack range of 50° to 60° for both Mach 6 and 10; and (3) at Mach 10 and $\alpha = 40°$, the pitching moment from an ideal-gas (Gas Model A) computation is in good agreement with experimental data (Fig. 6). However, the pitching

moment from a real-gas (Gas Model D) computations [3, 9] is in good agreement with the OADB value, which is based on flight data.

The present computations and the existing set of calculations [3] clearly demonstrate the ability of CFD to accurately predict shuttle aerodynamics at angles of attack up to 60° in ideal gas, as validated by flight (Mach 3.5 and 6) and ground-based testing (Mach 6 and 10). In addition, the aerodynamics predicted by the real-gas computations [3] at Mach 10 and 15 were validated up to $\alpha = 40°$ with flight data. The remaining validation work that is desired is the real-gas aerodynamics at higher ($\alpha > 40°$) angles of attack.

Real-Gas Effects

A common misperception is that real-gas effects are linked to the freestream Mach number. In reality, real-gas effects depend on both freestream enthalpy and density and manifest themselves in two ways – (1) as changes in shock-layer γ (ratio of specific heats) due to constituent gases being calorically imperfect (i.e., the specific heat of each constituent species is a function of temperature), and (2) as changes in the shock-layer gas composition because of chemical reactions which in turn change the effective shock-layer γ. The first effect occurs even at moderately low hypersonic flight Mach numbers ($M\infty \approx 6$). This is due to the temperature rise across the bow shock, which in turn causes the heat capacity (and equivalently γ) to change in the shock layer. Note that the two processes are sequential, i.e., the second effect (due to chemical changes) follows the first. The diatomic species in the shock-layer are first vibrationally excited before dissociating into component atoms. The change in chemical composition changes the heat capacity of the mixture and hence γ.

To illustrate these phenomena and their impact on the vehicle aerodynamics, an incremental approach has been taken in the present work. At an angle of attack of 60°, four separate computations are performed for Mach 6 and 15. The first computation uses the ideal-gas ($\gamma=1.4$) model (Gas Model A) which was used for all Mach 3.5 and 6 cases in the previous effort.3 The second computation uses a 5-species nonreacting air model (Gas Model B) in which the diatomic molecules (N_2 and O_2) are considered to be rigid rotors. The value of γ for this mixture is also 1.4 and, barring small differences in the modeling of the transport properties, this model should yield results that are identical to those for the ideal-gas model. The third computation also uses a 5-species nonreacting air model (Gas Model C). However, in this model the diatomic species are considered to be simple harmonic oscillators. Consequently, γ depends on the local temperature and varies not only across the shock but also through the entire shock layer. The fourth computation uses Gas Model D, which includes the effects of varying γ due to both temperature and gas composition (chemical reactions). This model was used for all Mach 10 and 15 cases in the previous effort [3].

The contours of computed surface pressure coefficients obtained using these four gas models are compared in Fig. 7. The results are arranged in two columns – the left column

shows the results of the Mach 6 computations and the right column shows the results of the Mach 15 computations. Each contour plot compares the results of two gas models. These plots highlight the areas where the surface pressure is affected by the gas model used. This approach is more informative than relying solely on differences in integrated aerodynamic coefficients, since it is possible that differences could be masked (due to offsetting errors) when the surface pressures are integrated to obtain the aerodynamics.

First consider the Mach 6 computations. As expected, Gas Models A and B yield identical results (Fig. 7a). From this result it can be concluded that there is consistency in the numerical implementation of the two physical models – 5 partial differential equations in the ideal gas set vs. the expanded 9 partial differential equations (4 additional species mass conservation equations) of a 5-species mixture. The thermodynamics of the two gas models are the same although implemented in two seemingly different ways. The effect of varying γ is evident in Fig. 7b in which the results from Gas Models B and C are compared. There is some change in the pressure distribution in the nose region and over the wing region. The impact of both chemical reactions and varying γ (Gas Model D) is shown in Fig. 7c. The pressure distributions are virtually identical for Gas Models C and D, which suggests that chemical reactions are not important at this Mach number in flight. The changes due to varying γ should not come as a surprise. At Mach 6 flight conditions, the temperature rise across the bow shock is sufficient to excite the vibrational modes of the diatomic constituents. This phenomenon will not be observed in the Mach 6 tunnel (and even the Mach 10 tunnel) because the freestream enthalpies are very low.

Next consider the Mach 15 computations. As in the Mach 6 computations, Gas Models A and B yield almost identical pressure distributions on the windward surface (Fig. 7d). Clear differences are seen in the results of Gas Models B and C (Fig. 7e). Differences are seen in the nose region, at the extremities of the wing, and in the body flap region. These differences are due to changes in γ – changes associated with the temperature rise across the bow shock. Unlike the Mach 6 computations, further differences are seen in the results of Gas Models C and D (Fig. 7f). The addition of finite-rate chemistry into the gas model significantly changes the pressure distribution. The values of the computed vehicle pitching moment coefficients are also shown in Figs. 7a–7f. From the differences in the values, the effect of the various gas models is clearly seen.

The vehicle pitching-moment coefficients computed using the ideal gas and 5-species nonequilibrium air models, are plotted as a function of angle of attack in Figs. 8a, 8b, and 8c for the Mach 6, 10, and 15 cases respectively. Also shown in the figures are the corresponding OADB values. The first observation made is that the ideal-gas model predicts a reversal in pitching moment (for $50° \leq \alpha \leq 60°$) for all three Mach numbers. Further, the ideal-gas pitching moment coefficients exhibit a second reversal at $\alpha > 60°$ (see Figs. 8b and 8c). This second reversal is consistent with experimental observations of Spencer and Calloway [12] who measured the 0.00986-scale Orbiter aerodynamic forces and moments in the angle-of-

attack range of 20°-90° for supersonic Mach numbers ranging from 1.8 to 4.6. The second observation is that real-gas effects generally produce more positive (nose-up) moments relative to ideal-gas values for angles of attack less than 50°. This observation is consistent with the findings from the earlier computations of Griffith et al. [5] Beyond 50°, real-gas effects produce more negative (nose down) pitching moments than the ideal-gas values, i.e., the pitching moment curves from ideal- and real-gas computations cross in the angle-of-attack range of 50° to 60°. More importantly, the pitching moment reversals seen in the ideal-gas computations and the OADB at Mach 10 and 15 are not observed in the real-gas computations. Even at Mach 10 there is significant difference between real-gas calculations and OADB data. Additionally, the fact that the ideal-gas computations at Mach 10 reproduce the same trends as those observed in NASA LaRC Mach 10 (air) experimental data, and the fact that the real-gas computations replicate flight/OADB data at α = 40°, strongly suggest that the pitching moment at high angles of attack (α > 40°) will depend on real-gas effects.

The findings of the present work are further bolstered by the results of completely independent computations at Mach 10 and 15 [16]. In these inviscid computations, an equilibrium air model was used in a three-dimensional, unstructured volume mesh generated using *FELISA* [17]. The results of these independent computations are in good agreement with the present results as shown in Figs. 8b and 8c.

Heuristic Arguments

The results of the ideal-gas computations at Mach 6, 10, and 15 clearly show a reversal in pitching moment. This reversal is also seen in the OADB values at all Mach numbers. In contrast, the corresponding real-gas computations show a delayed reversal at Mach 6 and very little (or none at all) at Mach 10 and 15. A clue to rationalizing this behavior lies in the procedure used to construct the OADB itself. During the development of the Orbiter Aerodynamic Design Database (ADDB) in the 1970s, the following observation was made (see page 5.1.3-6 of Ref. 13) from the extensive experimental data available at that time – at a given Mach number, the angle of attack at which a reversal in the Orbiter pitching moment would occur was approximately the maximum semi-vertex angle of a sharp cone for which an attached shock was possible. The attached shock is straight, i.e., a conical ray in the Taylor-MacColl solution [18]. The basic idea behind this heuristic argument (so called shock-detachment theory) stems from the fact that beyond the maximum flow turning angle, the shock detaches from the sharp body and a large subsonic zone develops in the shock layer. This subsonic zone "pushes" up against the shock causing the shock to acquire a streamwise curvature.

Figure 9a shows the maximum flow turning angle (same as the semi-vertex angle) for a sharp wedge and a sharp cone as a function of the freestream Mach number. The data are shown for an ideal gas (γ=1.405). The maximum flow turning angles for a sharp wedge are directly obtained from the following formula [19]

$$\sin^2 \theta_{\delta_{max,Wedge}} = \frac{1}{4\gamma M_\infty^2} \left\{ (\gamma+1)M_\infty^2 - 4 + \sqrt{(\gamma+1)\left[(\gamma+1)M_\infty^4 + 8(\gamma-1)M_\infty^2 + 16\right]} \right\} \qquad (1)$$

For a sharp cone, the maximum flow turning angles were extracted from the chart in Ref. 19. The solid and dashed lines in the figure are curve fits to the discrete data for a cone and wedge, respectively. Also shown in Fig. 9a are the experimental values (in low-enthalpy tunnels in which the working medium is an ideal gas) of angle at attack at which a reversal in pitching moment was observed. Note that the ratio of the maximum turning angles for a sharp cone and wedge asymptotically reaches a value of ≈1.26 as the Mach number approaches infinity. This ratio is always greater than unity because the sharp cone can sustain a higher turning angle than the wedge due to the three-dimensional relief the cone provides to the flow. Another observation made from the distribution of the experimental data, which only went as high as Mach 10, was that the angle of attack at pitching moment reversal reached an asymptotic value of ≈55° beyond Mach 5 (see Fig. 5.1.3-51 of Ref. 13). This value was then used in the OADB as the angle of attack at which pitching moment reversal would occur for all hypersonic Mach numbers. However, this argument failed to account for was real-gas effects and their impact on the maximum flow turning angle for a sharp cone. This shortcoming can be addressed through simple analytical arguments and verified through computations.

The maximum flow turning angle for a sharp wedge can be computed from Eq. (1) for several values of γ and M_∞. Since Ref. 19 provides a chart only for $\gamma = 1.405$, the maximum flow turning angle for a sharp cone is computed assuming that the ratio of wedge to cone turning angles is not a function of γ. The family of curves that result for Mach 6, 10, and 15 are shown in Fig. 9b – the maximum flow turning angle for a sharp cone is plotted as a function of γ. Also shown in Fig. 9b are the limiting curves for $M_\infty \to \infty$. Two observations are made – (1) for a given M∞, the maximum flow turning angle increases with decreasing γ, and (2) for a given value of γ, the maximum flow turning angle increases with M_∞. A reasonable assumption is that the γ value that controls the maximum flow turning angle is the lower post-shock value and not the freestream value. The results from these simple analytical arguments suggest that, at hypersonic speeds in flight, pitching moment reversal would occur at a much higher angle of attack than the value of 55° used in the OADB.

This argument is verifiable through computations, which can be easily performed for sharp cones. A series of inviscid computations were performed at Mach 15 for sharp cones of semi-vertex angles 50°, 60°, and 70°. A value of 3.281 ft was used as the base radius for each cone with a shoulder radius of 0.3281 ft. The shoulder was necessary to anchor the sonic line and ensure a supersonic outflow. Gas Models A, C, D, and E were used in the computations – the choice of Gas Model E will be justified in a later section of the paper. The pitch plane contours of Mach number for each gas model and cone angle are shown in Fig. 10.

For a 50° cone, the ideal-gas solution predicts an attached shock, as expected. The real-gas solutions from Gas Models C and D also predict an attached shock with the shock moving inward (i.e., towards the body). Note that there is little difference in these two solutions. For a 60° cone, the ideal-gas solution shows the development of streamwise curvature in the bow shock. Note that at Mach 15, the theoretical maximum flow turning angle for a sharp cone is roughly 57.5°.19 The results from Gas Models C and D predict an attached shock. The impact of chemical reactions (Gas Model D) is clearly seen in the Mach number contours. The outer shock moves further inward compared to the results from Gas Model C (varying γ only). For the 70° cone, the ideal-gas solution clearly shows shock detachment as does the solution from Gas Model C. The solution from Gas Model D for this cone angle appears similar to the ideal-gas 60° solution, i.e., the beginnings of shock detachment. We note in passing that the shock shapes predicted for Gas Model E (CF4) mimic those for Gas Model D (5-species reacting air). This observation will prove useful in a later section.

The preceding discussion and results indicate that one should expect a reversal in pitching moment in the angle-of-attack range of $50° \leq \alpha \leq 60°$ for an ideal gas, and in the range of $60° \leq \alpha \leq 70°$ for a real gas. Returning to Fig. 8c (C_m vs α for Mach 15), the reversals in pitching moment can be clearly seen in these ranges for the ideal- and real-gas cases. For the real-gas case, however, the reversal is less pronounced.

Experimental Verification of Real-Gas Aerodynamics

The results of the series of ideal- and real-gas computations performed in the present work clearly demonstrate the strong dependence of the vehicle pitching moment on real-gas effects. Further, the results suggest the reversal in the vehicle pitching moment at Mach 15 (and perhaps even at Mach 10) will occur (if at all) at an angle of attack larger than 60°. Since the Orbiter does not attain these attitudes during nominal flight and it is not prudent to recommend a flight experiment, an alternate verification method is desired. The possibility of performing confirmatory experiments in ground-based facilities is examined next.

The existing wind-tunnel facilities with air as the working medium cannot simulate a varying γ environment since their stagnation enthalpies are extremely low (the post-shock temperature is not of sufficient magnitude to change γ appreciably). However, further tests at high angles of attack ($50° \leq \alpha \leq 70°$) in the Mach 6 and 10 facilities at NASA LaRC would provide valuable data to establish the validity of the ideal-gas results presented in the current paper and to account for Mach number effects. Note that the wind tunnel tests of Spencer and Calloway [13] did cover the high angle of attack regime however, test Mach numbers were less than 4.5.

In order to examine the validity of the real-gas pitching moment at high Mach number and high angle of attack, another experimental facility must be considered. A 20-inch Mach 6 tunnel at NASA LaRC uses a heavy gas (CF4) whose γ has a strong dependence on

temperature. Further, the γ value of CF_4 is close to 1.2, which is a typical value for high-temperature air. This similarity in γ has been exploited in the past for the Aeroassist Flight Experiment20 and Space Shuttle programs.15 Further, the inviscid computations performed for a sharp cone using the Gas Model E (CF_4) yielded results that showed strong similarities with those from Mach 15 computations for 5-species air. The premise is then, the pitching moments obtained from CF_4 computations will mimic the angle of attack behavior as those from 5-species air computations, i.e., we can expect a weak reversal in pitching moment in the angle-of-attack range $60° \leq \alpha \leq 70°$.

Several laminar solutions are computed over a 0.004-scale model for the freestream conditions given in Table 2 and angles of attack given in Table 3. Note that the angle-of-attack resolution is increased in the range of 60° to 70° through 2° increments. At an angle of attack of 60°, contours of the surface pressure coefficients, obtained using a 5-species chemical nonequilibrium air model at Mach 15 and CF_4 gas at Mach 6, are compared in Fig. 11a. The contours are quite similar except in the region around the reference axis (≈ 0.65 x/L_B). For the entire angle-of-attack range ($20° \leq \alpha \leq 70°$), the computed pitching moment coefficients are compared against the experimental data in Fig. 11b. The OADB values (at Mach 15) of the corresponding coefficients are also shown in the figures. The computed values of pitching moment closely follow the experimental trend up to $\alpha = 45°$ (the experimental limit). The interesting aspect of the computations is the near agreement (in both value and trend) between the CF_4 results and those of Mach 15 air. Note that between the range of 60° and 70°, the Mach 6 CF_4 computations have been performed with a 2° increment in angle of attack, as opposed to an unevenly spaced distribution for Mach 15 air. The pitching moment coefficients obtained from both computations show a small inflection between $66° \leq \alpha \leq 70°$. This strongly suggests that there might not be any observable reversal in pitching moment at very high Mach numbers. Further tests at high angles of attack in this unique facility at NASA LaRC would not only yield valuable data for CFD code validation but will also verify the presence of pitching moment reversal in a flow medium that mimics high-temperature air.

Summary and Conclusions

Laminar three-dimensional computations were performed using *GASPex* [6] for Shuttle Orbiter at three representative points – Mach 6, 10, 15 and for angles of attack ranging from 0° to 70°. Both ideal-gas (γ=1.4) and real-gas (5-species chemical nonequilibrium air) models were used in the computations. The primary focus of the present work was to quantify vehicle pitching moment coefficient and its reversal at high angles of attack.

The aerodynamic data obtained from coarse-grid Mach 6 and 10 computations using an ideal gas model were compared against experimental data from different ground-based facilities. The computed results were found to be in good agreement with measured data and follow experimental trends very well. Further, the pitching moment coefficients extracted

from the ideal-gas solutions at Mach 6, 10, and 15 clearly showed a reversal in the angle-of-attack range $50° \leq \alpha \leq 60°$.

The impact of real-gas effects was demonstrated through an incremental approach at two computational points – Mach 6 and 15 for an angle of attack of 60°. The complexity of the gas model in these computations ranged from a single species gas of constant γ (ideal gas) to a 5-species reacting mixture of imperfect gases. The impacts of varying γ, as well as chemical reactions, on the pitching moment were also presented. The real-gas calculations showed that the reversal in pitching moment was much less pronounced, and occurred at a higher angle of attack than predicted in the OADB.

The location of a pitching moment reversal in the OADB was based on the shock detachment argument, i.e., the angle of attack at which pitching moment reversal would occur is approximately the maximum flow turning angle of a sharp cone for which an attached shock is possible. This heuristic argument from the 1970s was put to the test at Mach 15 through inviscid, ideal- and real-gas computations for sharp cones of angles 50°, 60°, and 70°. The ideal-gas results verified this argument – the Orbiter pitching moment reverses in the range $50° \leq \alpha \leq 60°$ for an ideal gas. The real-gas results from the sharp cone computations indicated a shock detachment in the range $60° \leq \alpha \leq 70°$, which matched results from laminar computations for the Orbiter. The simple mathematical extension of the heuristic argument through varying γ also indicated the same behavior.

The possibility of experimentally verifying the results at Mach 15 was explored. Since low-enthalpy ground-based test facilities that use air as the working medium cannot replicate real-gas effects, the idea of using a heavier, polyatomic gas (such as CF_4 – NASA LaRC Mach 6 Tunnel) was tested. Laminar three-dimensional computations were performed for an angle-of-attack range of 20° to 70°. The results of computations showed fair agreement with experimental data. More importantly, the results at high angles of attack exhibited behavior similar to that of air at Mach 15. These computations establish the viability of aerodynamic testing in CF_4.

The confidence gained from the present analysis offers the exciting possibility of performing additional computations to determine precisely the combinations of control surface deflections necessary to trim (statically) the vehicle at high angles of attack. Further, the present work can be extended to study the interference effects of elevons and body flaps and their impact on both vehicle aerodynamics and hinge moments. A preliminary effort in this direction was established in Ref. 9.

To summarize the present work, the reversal in pitching moment strongly depends on the choice of gas model. The heuristic argument used in the current OADB is verified for the case of an ideal gas. The same heuristic argument for a real-gas shows a delay in reversal of the pitching moment. The argument is also consistent with the results of the CFD computations.

Acknowledgements

References

1. Ondler, M., "Abort Improvement Team Recommendation," PRCB SR 1145A, NASA Johnson Space Center, Dec. 1999.

2. Boeing, Human Space Flight and Exploration, Huntington Beach, CA, "Operational Aerodynamic Data Book," Boeing Document STS85-0118 CHG 9, 2000.

3. Papadopoulos, P.E., Prabhu, D., Wright, M.J., Davies, C.B., McDaniel, R.D., Venkatapathy, E., Wercinski, P., and Gomez, R.J., "CFD Simulations in Support of Space Shuttle Orbiter Contingency Aerodynamic Database Enhancement," AIAA Paper 2001-3067, June 2001.

4. Woods, W.C., Arrington, J.P., and Hamilton, H.H., II, "A Review of Preflight Estimates of Real-Gas Effects on Space Shuttle Aerodynamic Characteristics," in Orbiter Experiments (OEX) Aerothermodynamics Symposium, edited by D.A. Throckmorton, NASA CP-3248, Part 1, 1995, pp. 309–346.

5. Griffith, B.J., Maus, J.R., and Best, J.T., "Explanation of the Hypersonic Longitudinal Stability Problem – Lessons Learned," in Orbiter Experiments (OEX) Aerothermodynamics Symposium, edited by D.A. Throckmorton, NASA CP-3248, Part 1, 1995, pp. 347–380.

6. AeroSoft, Inc., 1872 Pratt Drive, Suite 1275, Blacksburg, VA 24060-6363, *GASPex Version 3 User's Manual*, 1997.

7. Prabhu, D.K., Wright, M.J., Marvin, J.G., Brown, J.L., and Venkatapathy, E., "X-33 Aerothermal Design Environment Predictions: Verification and Validation," AIAA Paper 2000-2686, June 2000.

8. Loomis, M.P., Venkatapathy, E., Papadopoulos, P., Davies, C. B., Berry, S., Horvath, T., and Campbell, C., "Aeroheating and Aerodynamic CFD Validation and Prediction for the X-38 Program," AIAA Paper 97-2478, June 1997.

9. Prabhu, D.K., Papadopoulos, P.E., Davies, C.B., Wright, M.J., McDaniel, R.D., Venkatapathy, E., and Wercinski, P.E., "Shuttle Orbiter Abort Aerodynamics, II: Real-Gas Effects and High Angles of Attack," AIAA Paper No. 2003-1248, January 2003.

10. Blottner, F.G., Johnson, M., and Ellis, M., "Chemically Reacting Viscous Flow Program for Multi-Component Gas Mixtures," Report SC-RR-70-754, Sandia Laboratories, Albuquerque, NM, December 1971.

11. Svehla, R.A, "Estimated Viscosities and Thermal Conductivities of Gases at High Temperatures," NASA TR-R-132, 1962.

12. Romere, P.O., and Brown, S.W., "Documentation and Archiving of the Space Shuttle Wind Tunnel Test Data Base," NASA-TM 104806, Vol. 2, Jan. 1995.

13. Space Division, Rockwell International, "Aerodynamic Design Substantiation Report, Volume 1: Orbiter Vehicle," Report No. SD74-SH-0206, Volume 1L, December 1978.

14. Paulson, J.W., Jr., and Brauckmann, G.J., "Recent Ground-Facility Simulations of Shuttle Orbiter Aerodynamics," in Orbiter Experiments (OEX) Aerothermodynamics Symposium, edited by D.A. Throckmorton, NASA CP-3248, Part 1, 1995, pp. 283–307.

15. Spencer, B, Jr., and Calloway, R.L, "Supersonic Aerodynamic Characteristics of a Space Shuttle Orbiter Model at Angles of Attack from 20° to 90°," NASA TM-89112, July 1987.

16. Prabhu, R.K., "Inviscid Flow Computations of the Shuttle Orbiter for Mach 10 and 15 and Angle of Attack 40 to 60 degrees," NASA/CR–2001–211267, Dec. 2001.

17. Peiro, J., Peraire, J., and Morgan, K., "FELISA System Reference Manual and User's Guide," Tech. Report, University College of Swansea, Swansea, UK, 1993.

18. Anderson, J.D., Jr., *Modern Compressible Flow: with Historical Perspective*, McGraw-Hill, New York, 1982.

19. Anon., "Equations, Tables, and Charts for Compressible Flow," NACA Report 1135, NASA Ames Research Center, 1953.

20. Micol, J.R., "Simulation of Real-Gas Effects on Pressure Distributions for Aeroassist Flight Experiment Vehicle and Comparison with Predictions," NASA TP-3157, 1992.

Table 1. Physical models and numerical algorithms used in *GASPex* (v3.2.4) [Ref. 9]

	Ideal-Gas Model	5-species Air Model	CF$_4$ Model
Thermodynamics	$\gamma = 1.4$	Eq. Stat. Mech.	Eq. Stat. Mech.
Laminar Transport			
Viscosity	Sutherland's Law	Blottner's Curve Fits	Blottner's Curve Fit
Conductivity	$Pr = 0.72$	Eucken's Relation	Eucken's Relation
Mass diffusion	–	Binary, $Sc = 0.7$	–
Chemical Kinetics	–	Park Rates	–
Inviscid Flux	Van Leer	Van Leer	Van Leer
Accuracy	3rd-Order (MUSCL)	3rd-Order (MUSCL)	3rd-Order (MUSCL)
Limiter	Minmod	Minmod	Minmod
Viscous Flux	Central	Central	Central
Accuracy	2nd-Order	2nd-Order	2nd-Order
Wall BC	Isothermal wall (T_w=2160 °R)	Isothermal wall (T_w=2160 °R)	Isothermal wall (T_w=540 °R)
Time Integration	2-Factor AF	2-Factor AF	2-Factor AF

Table 2 Freestream conditions for flight and wind tunnel cases [Ref. 9]

Z (kft)	T_∞ (°R)	ρ_∞ (slugs/ft^3)x10^{-7}	M_∞	V_∞ (ft/sec)	q_∞ (psf)	α	Re_∞ (1/ft)x10^{-6}
Flight Cases (Air)
135	456.11	65.6	6	6,280.1	129.5	0°–65°	0.122
140	463.68	52.8	10	10,553.3	295.3	20°–70°	0.164
190	454.73	7.77	15	15,708.8	95.88	0°–70°	0.036
Wind Tunnel Cases (CF$_4$ gas)
0	306.00	343	6	2,778.1	132.53	0°–70°	0.385

Table 3 Angle-of-attack schedule for various gas models [Ref. 9]

M_∞	Ideal-Gas (Gas Model A: $\gamma = 1.4$)	Real-Gas (Gas Model D: 5-sp. air)	Real-Gas (Gas Model E: CF$_4$)
6	0°–20° ($\Delta\alpha = 5°$), 20°–50° ($\Delta\alpha = 10°$), 50°–60° ($\Delta\alpha = 2°$)	20°–50° ($\Delta\alpha = 10°$) 50°–60°[a] ($\Delta\alpha = 2.5°$)	20°–60° ($\Delta\alpha = 5°$), 60°–70° ($\Delta\alpha = 2°$)
10	20°–50° ($\Delta\alpha = 10°$), 50°–60° ($\Delta\alpha = 2°$), 65°, 70°	30°–60° ($\Delta\alpha = 10°$) 60°–70° ($\Delta\alpha = 2.5°$)	
15	20°–50° ($\Delta\alpha = 10°$), 50°–60° ($\Delta\alpha = 2°$), 65°, 70°	30°–60° ($\Delta\alpha = 10°$) 60°[a]–70° ($\Delta\alpha = 2.5°$)	

[a] Additional computations at $\alpha = 60°$ using Gas Models B and C
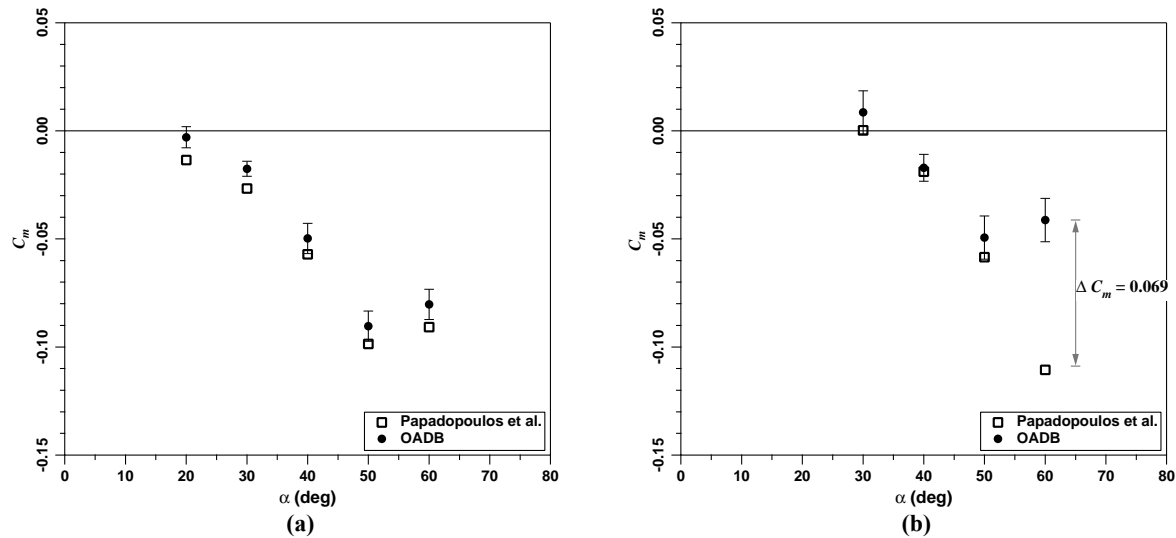
Figure 1. Vehicle pitching moment coefficients computed by Papadopoulos *et al.* (Ref. 3) compared to corresponding values in the OADB for – (a) Mach 6, Z=135 kft, $\delta_E = \delta_{BF} = 0°$, $\delta_{SB} = -69.76°$, Gas Model A, Turbulent flow, and (b) Mach 15, Z=190 kft, $\delta_E = \delta_{BF} = \delta_{SB} = 0°$, Gas Model D, Laminar flow. For the Mach 6 case, a reversal in the vehicle pitching moment is observed at $\alpha > 50°$, however, a similar reversal at Mach 15 is not predicted by the computations.
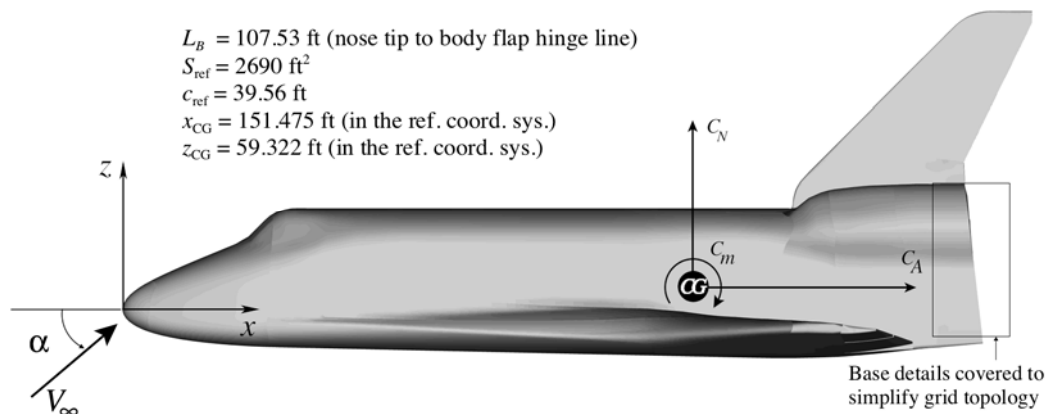
Figure 2. Space Shuttle Orbiter configuration, moment center (CG) location, and sign conventions for positive aerodynamic forces (C_N and C_A) and moments (C_m). The CG is offset from both the x and z axes. For the configuration shown, the control surfaces are undeflected, i.e., $\delta_E = \delta_{BF} = \delta_{SB} = 0°$.
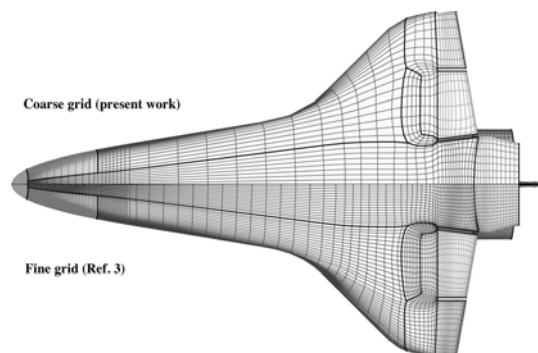
Figure 3. Comparison of the coarse (present work) and fine surface grids (Ref. 3). The control surfaces are undeflected, i.e., $\delta_E = \delta_{BF} = \delta_{SB} = 0°$.
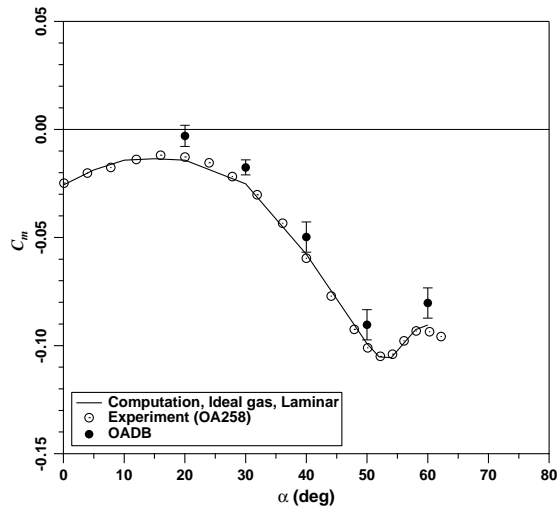
Figure 4. Comparison of computed pitching moment coefficients with experimental data ($M_\infty = 6$, 0.02-scale model) from the OA258 wind-tunnel experiment performed in the AEDC Von Kármán Tunnel B (Ref. 13).
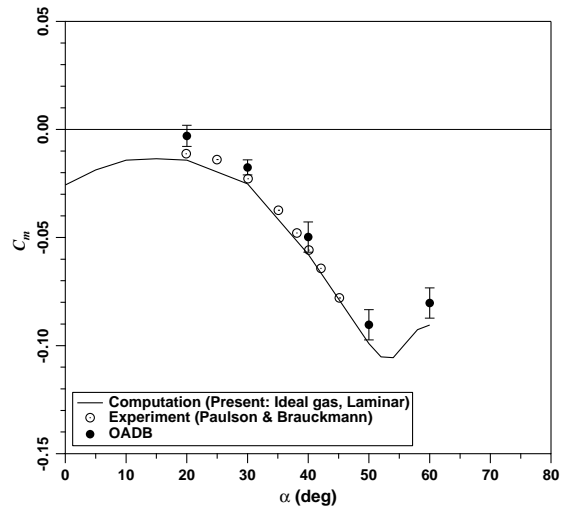

Figure 5. Comparison of computed pitching moment coefficients with experimental data ($M_\infty = 6$, 0.004-scale model) from the NASA LaRC 20-inch Mach 6 Air Tunnel (Ref. 14).
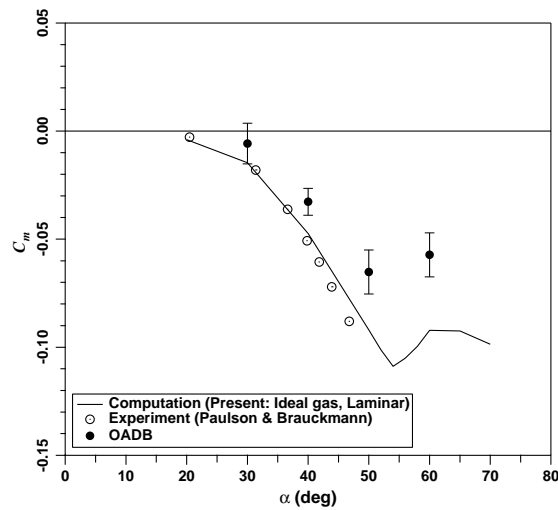

Figure 6. Comparison of computed pitching moment coefficients with experimental data ($M_\infty = 10$, 0.0075-scale model) from the NASA LaRC 31-inch Mach 10 Air Tunnel (Ref. 14).
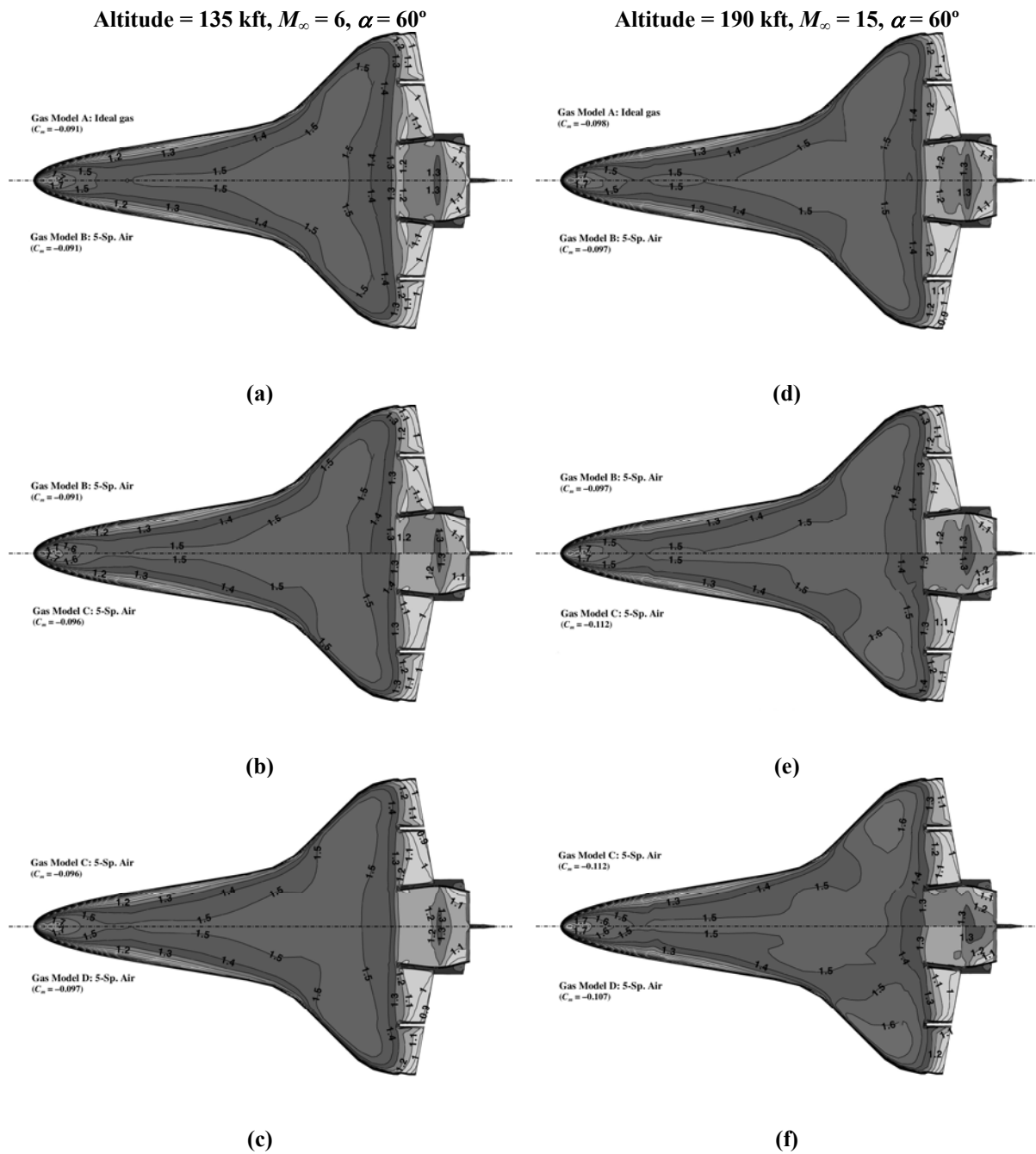
Altitude = 135 kft, $M_\infty = 6$, $\alpha = 60°$ **Altitude = 190 kft, $M_\infty = 15$, $\alpha = 60°$**

(a)   (d)

(b)   (e)

(c)   (f)

Figure 7.   Comparison of windside surface pressure coefficient contours for four different gas models – (1) Gas Model A: ideal gas ($\gamma = 1.4$), (2) Gas Model B: nonreacting (frozen) mixture of ideal gases, (3) Gas Model C: nonreacting (frozen) mixture of calorically imperfect gases, and (4) Gas Model D: chemically reacting (finite-rate) mixture of calorically imperfect gases – for Mach 6 (7a-7c) and Mach 15 (7d-7f). The control surfaces are in their undeflected positions, i.e., $\delta_E = \delta_{BF} = \delta_{SB} = 0°$, and the flow is assumed to be laminar. The values of the computed pitching moment coefficients are also shown.
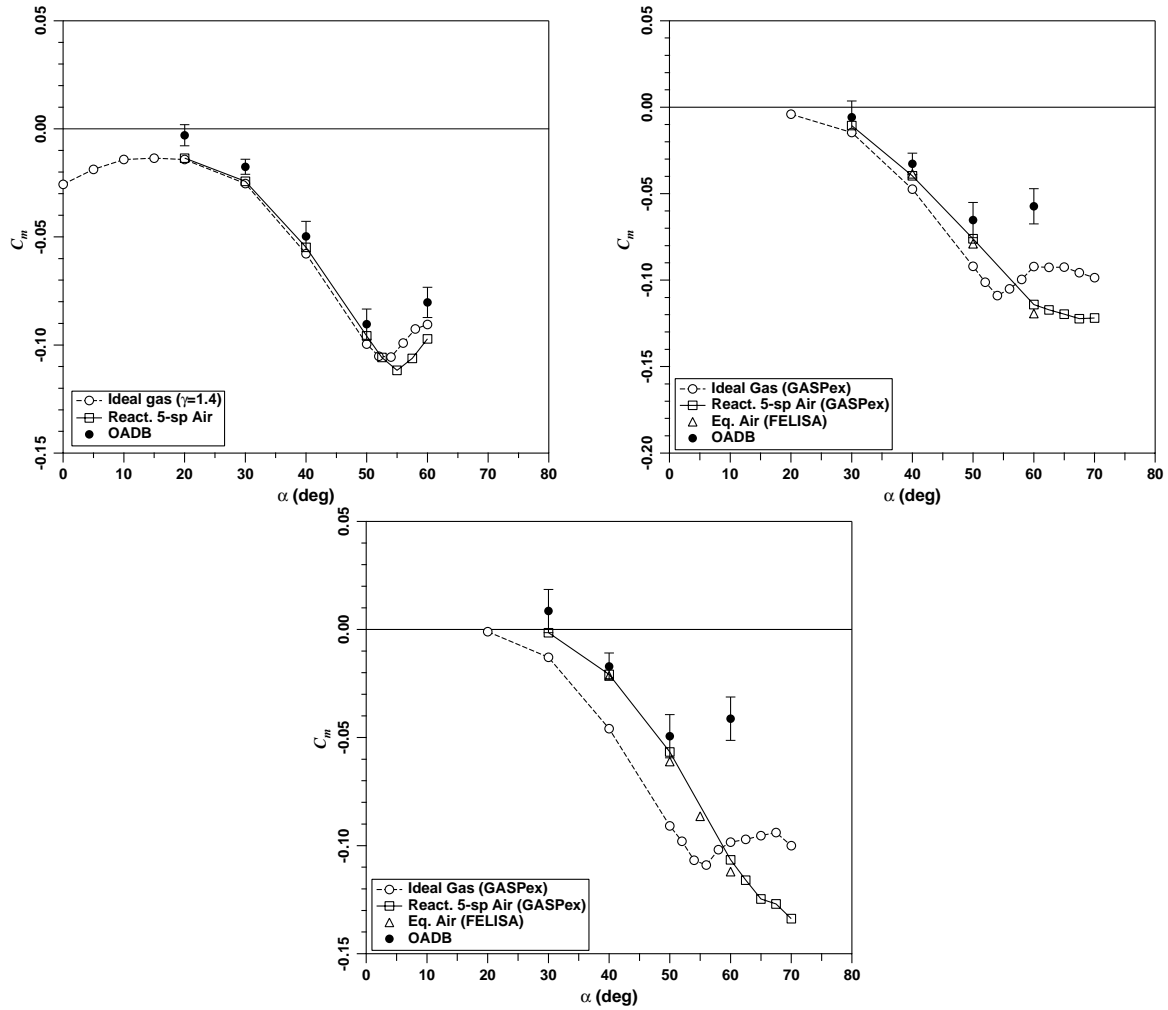
Figure 8.   Comparison of pitching moment coefficients – (a) Z = 135 kft, M_∞ = 6, (b) Z = 140 kft, M_∞ = 10, and (c) Z = 190 kft, M_∞ = 15, laminar flow computations for ideal-gas (Gas Model A), real-gas (Gas Model D: 5-species Air) models, and equilibrium air (Ref. 16). The control surfaces are undeflected in all the computations, i.e., $\delta_E = \delta_{BF} = \delta_{SB} = 0°$.
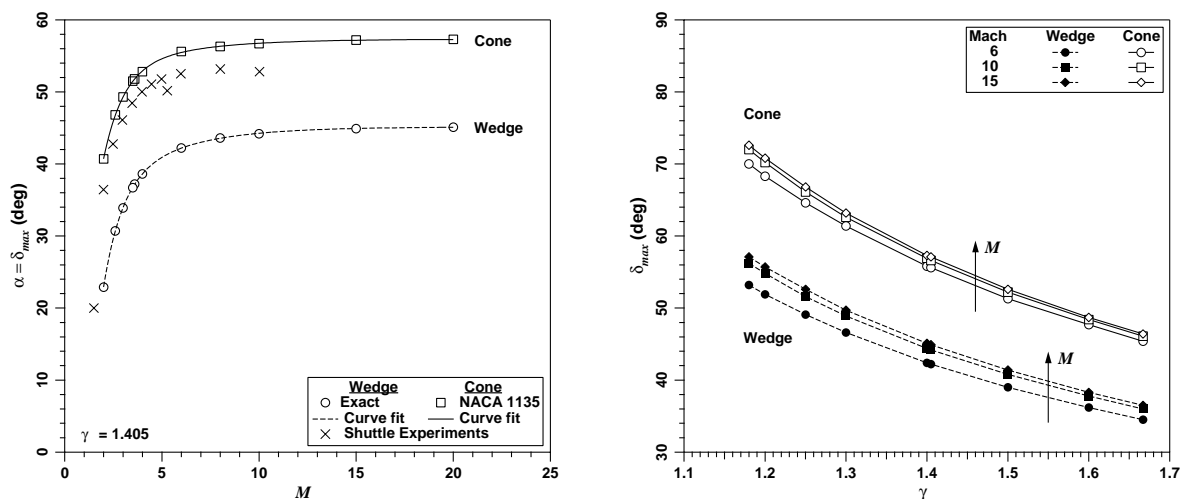

Figure 9.   Maximum flow turning angle (δ_{max}) for an attached shock for a wedge and a cone (γ_∞=1.405) as a function of – (a) freestream Mach number, and (b) freestream isentropic exponent. The turning angles for a wedge are exact values while those for the cone are obtained from NACA 1135 (Ref. 19). The experimental values of Orbiter angle of attack at C_m reversal are extracted from Ref. 13.
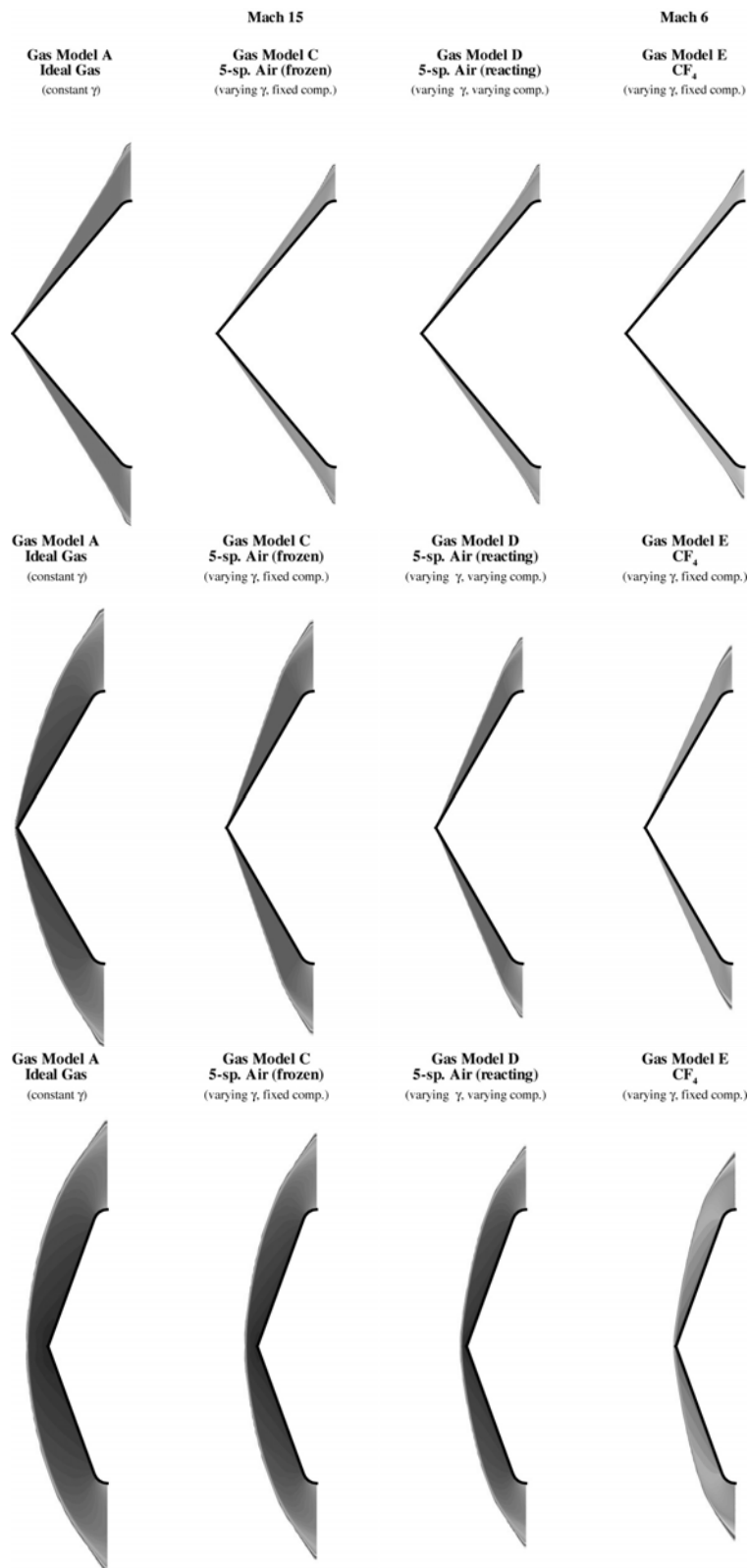
Figure 10.   Pitch plane Mach number contours for sharp cones of half angles – (a) $\theta_c = 50°$, (b) $\theta_c = 60°$, and (c) $\theta_c = 70°$ – from inviscid axisymmetric computations for various gas models (Gas Model A: ideal gas, Gas Model C: frozen mixture of perfect gases, Gas Model D: chemical nonequilibrium mixture of perfect gases, Gas Model E: CF_4).
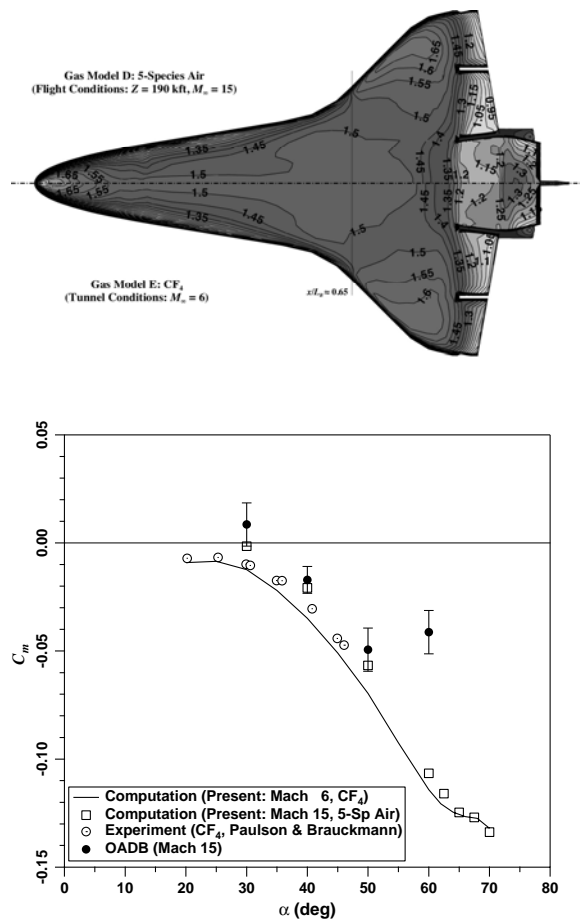
Figure 11. Comparison of – (a) windward distributions of pressure coefficient for Mach 15 5-species air (Gas Model D) and CF_4 (Gas Model E) for an angle of attack of 60°, and (b) computed pitching moment coefficients with experimental data (LaRC 20-inch Mach 6 CF_4 Tunnel). Experimental data are electronically extracted from Ref. 14.